Volume 12
Number 19
7 October 2025
Pages 7621–8218

Materials Horizons

rsc.li/materials-horizons

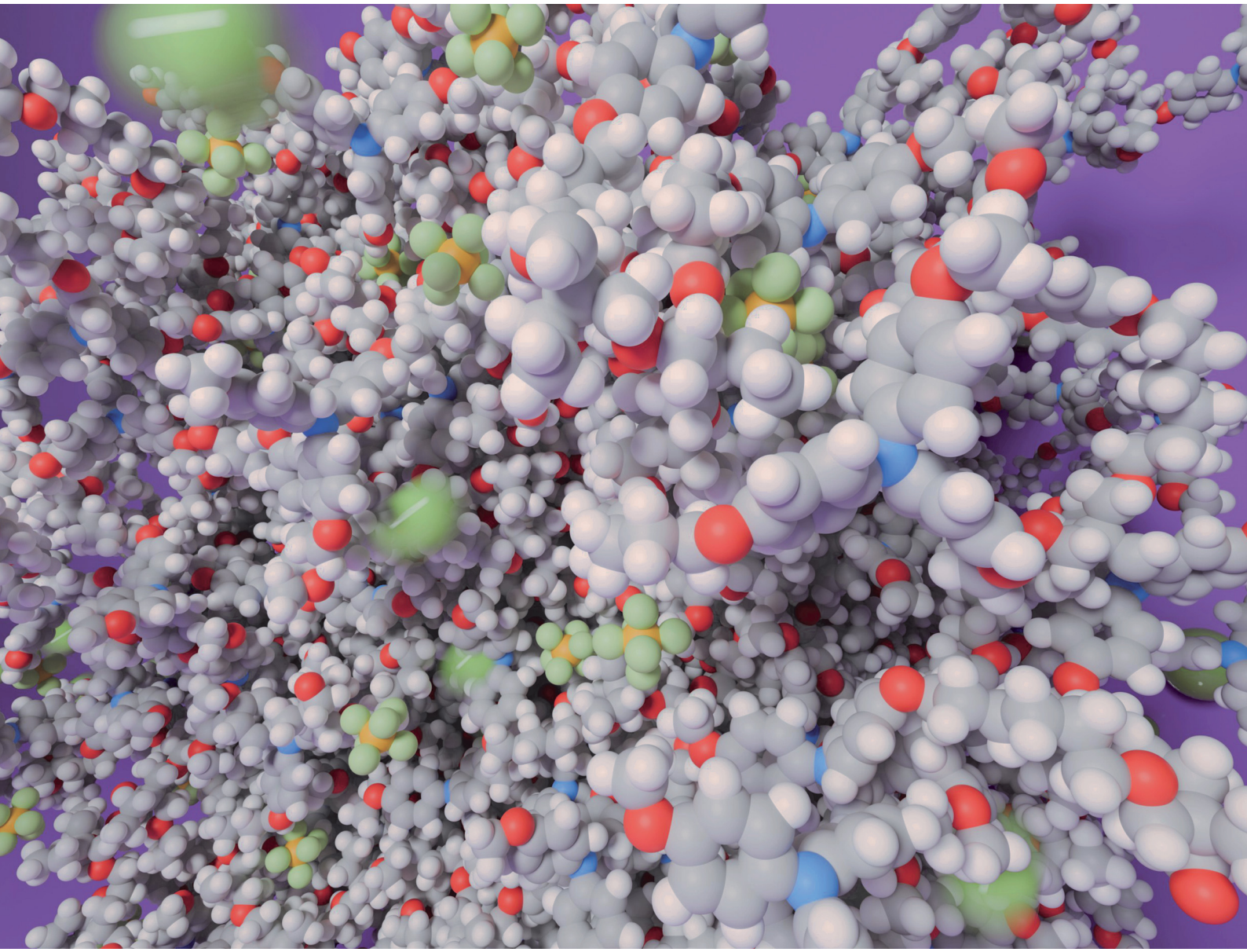

ISSN 2051-6347

ROYAL SOCIETY OF CHEMISTRY

COMMUNICATION

Klaus Meerholz, Daniele Fazzi *et al.*
Dynamics of disorder in mixed ionic–electronic transport in cross-linked non-conjugated redox polymers

Materials Horizons

ROYAL SOCIETY OF CHEMISTRY

COMMUNICATION

View Article Online
View Journal | View Issue

Check for updates

Cite this: *Mater. Horiz.*, 2025, **12**, 7924

Received 3rd April 2025,
Accepted 7th July 2025

DOI: 10.1039/d5mh00610d

rsc.li/materials-horizons

Dynamics of disorder in mixed ionic–electronic transport in cross-linked non-conjugated redox polymers†

Robert Herzhoff, [a] Laura Plein, [a] Alessandro Troisi, [b] Klaus Meerholz *[a] and Daniele Fazzi *[ac]

The coupled electronic and ionic transport mechanisms in organic mixed ionic–electronic conductors (OMIECs) remain elusive to rationalize. We introduce here an approach to model the entangled hole and ion transport in linear and cross-linked triphenylamine-based (TPA) non-conjugated polymers, studied as redox active materials for organic electrodes. The polymers are created *via* a heuristic method based on molecular dynamics (MD) simulations. Remarkable energetic disorder effects (up to 1.6 eV) are computed in the static limit, for both pristine and doped polymer films, seemingly hindering hole transport. The explicit inclusion of dynamic effects in modelling the energetic disorder leads instead to strong and rapid oscillations of the site-energies, thus enabling a dynamic opening of hole transport channels. To go beyond the static limit for the calculation of the hole transfer rates, encompassing the time-dependence of disorder effects, effective Marcus residence times are introduced for the first time. Distributions of charge escape times are derived for both linear and cross-linked polymers, in their pristine and doped states. Linear polymers show hole escape networks denser than cross-linked ones, suggesting a more efficient hole de-trapping developing as a function of time and disorder effects. Our approach shows that electronic transport in non-conjugated organic electrodes is a highly interdependent phenomenon connected to the bulk morphologies, polymer chain mobility and ion dynamics. A multiscale modelling that captures the dynamics of disorder is therefore indispensable.

New concepts

Dynamic effects, arising from the interplay between electronic charges, ions and molecular motions, govern the transport phenomena in organic mixed ionic–electronic conductors (OMIECs). Rationalizing such complex events, providing a mechanistic understanding at different length-scales, remains challenging due to the structural complexity of organic electrodes. Focusing on cross-linked non-conjugated redox polymers used as organic electrodes, we present a thorough bottom-up approach for modelling the coupled charge- and ion transport. We show how to generate *in silico* cross-linked bulk morphologies, leading to amorphous and porous structures allowing ion penetration and diffusion. We introduce a novel strategy to evaluate both static and dynamic disorder effects in the description of the electronic charge transport, by including the influence of polymer segments and ion motions. Our findings show how deep traps, caused by remarkable static energetic disorder, can be overcome by dynamical effects leading to efficient charge de-trapping and electronic transport. We suggest that the dynamics of disorder are the key to understand the origin of the transport mechanisms in organic electrodes.

Introduction

Organic mixed ionic–electronic conductors (OMIECs) are materials featuring both ionic and electronic conductivities.[1–4] Typical examples include conjugated small molecules (*e.g.*, naphthalene diimide (NDI)-based)[5–8] or polymers (*e.g.*, polythiophenes, poly(2-(4,4′-bis(2-methoxyethoxy)-5′-methyl-[2,2′-bithiophen]-5-yl)-5-methylthieno[3,2-*b*]thiophene) (pgBTTT), poly(3,4 ethylenedioxy-thiophene):polystyrene sulfonate (PEDOT:PSS), poly-(benzimidazobenzophenanthrolin) (BBL), *etc.*),[2,3,8–13] as well as non-conjugated materials like poly(4-glycidyloxy-2,2,6,6-tetramethylpiperidine-1-oxyl) (PTEO)[14] and they represent ideal active systems for a plethora of electrochemical applications, ranging from electrochemical energy storage (EES) devices (*e.g.*, secondary batteries and supercapacitors),[9,15–19] bioelectronics,[20] and optoelectronics,[21] as well as neuromorphic and sensing technologies.[22] Focusing on batteries, organic electrodes can represent an alternative to traditional electrodes commonly based on inorganic materials (*e.g.*, lithium transition metal oxides and nickel–manganese–cobalt-oxides (NMC)) or graphite.[23] Such systems show high energy density; however, they suffer from severe capacity loss due to the degradation of the crystal structure and they are reliant on non-renewable resources.[24] Organic electrodes

[a] *Institut für Licht und Materialien, Department für Chemie, Universität zu Köln, Greinstr. 4-6, 50939 Köln, Germany. E-mail: klaus.meerholz@uni-koeln.de, daniele.fazzi@unibo.it*
[b] *University of Liverpool, Department of Chemistry, Liverpool, L69 3BX, UK*
[c] *University of Bologna, Department of Chemistry 'Giacomo Ciamician', via P. Gobetti 85, 40129 Bologna, Italy*

† Electronic supplementary information (ESI) available. See DOI: https://doi.org/10.1039/d5mh00610d

can be a sustainable alternative,[25] however, depending on their chemical structure, they feature low specific capacity and energy density.[17] Thus, at the moment, they are rather complementary to the strengths of the inorganic counterparts.

Recent experimental and theoretical contributions from various research groups (*e.g.* Moia *et al.*,[9] Siemons *et al.*,[26] Keene *et al.*,[27,28] Sunny *et al.*,[29] Khot *et al.*,[30] Giovannitti *et al.*,[31] and Tsafati *et al.*[32]) showed that the bulk morphology of conjugated polymer-based OMIECs is highly affected by multiple factors, such as the flexibility of the polymer backbone, the nature of the side chains (*e.g.*, the amount and position of ether groups), and the ability to take in ions and solvent molecules. Changes in the morphology and ion uptake naturally influence the bulk transport properties, but a clear understanding about how ions and charge transport are coupled is still missing. Burke *et al.* and Landi *et al.* have underlined the importance of considering electrostatic disorder effects in modelling the electronic conduction mechanisms in conjugated polymers.[33,34] Their studies revealed that OMIECs are characterised by a large amount of static energetic disorder, represented by a broad distribution of the hopping site energies (ranging from 0.1 to 0.3 eV).[33] In accordance with the charge transfer theories for disordered (amorphous) materials (*e.g.*, Miller–Abrahams[35,36]), charge transport should not occur under high static energetic disorder conditions due to charge trapping in the tail states of the density of states, however this conclusion contradicts the experimental evidence.[37] Despite the large static disorder, charge transport in OMIECs can take place thanks to a favourable energy-level alignment of the hopping sites which develops in time, spontaneously arising from their fluctuations. It is, therefore, the dynamics of the system (*e.g.*, intra- and intermolecular vibrations, polymer segment mobility, and ion motion) which play a central role in organic electrodes and thus need to be included into any atomistic modelling strategy, since a static approach is insufficient to capture the transient nature of the charge transfer events.[33] Despite these findings, the understanding of the interrelated ionic and electronic charge transport in organic electrodes as well as the complex relationship between composition, morphology and transport properties remains limited.[4,28]

In this study, we address the above issues guided by the following questions: (i) what are the time scales characterising transport mechanisms in non-conjugated organic electrodes, that is the dynamics of disorder, (ii) how can we include both nuclear motions, across various time scales, and the charge transfer mechanisms into the charge transport description, and (iii) what are the consequences of different disorder effects (*e.g.*, structural, energetic, *etc.*) impacting the coupled ionic–electronic transport.

To answer the above questions, we model the pristine (*i.e.*, undoped) and doped (*i.e.*, charged‡) bulk morphologies for two redox-active non-conjugated triphenylamine (**TPA**) polymers (so-called redox polymers) *via* molecular dynamics (MD) simulations, encompassing the evaluation of the static and dynamic energy landscape, the rates of the electronic charge transport, and the ion diffusion. The **TPA** monomers, functionalized with

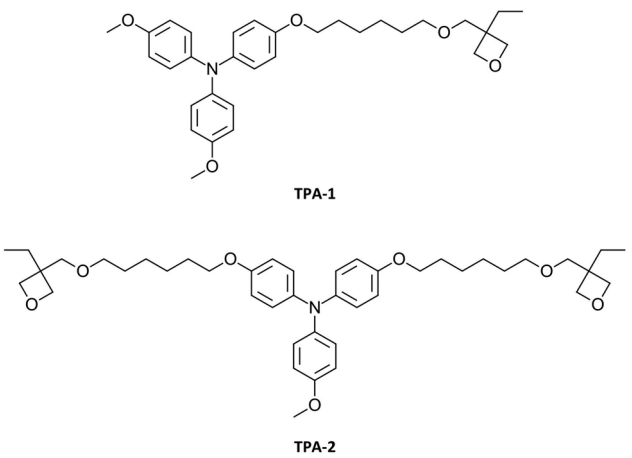

Fig. 1 Chemical structures of triphenylamine compounds with one (**TPA-1**, top) and two oxetane functionalities (**TPA-2**, bottom).

one (**TPA-1**) or two (**TPA-2**) oxetane-bearing sidechains, are shown in Fig. 1. They can be polymerized by cationic ring-opening polymerization (CROP), *e.g.* by using a photoacid generator as the proton source after UV-light irradiation, leading to the formation of a linear side-chain polymer (**pTPA**) or a cross-linked polymer network (**xTPA**).[38,39] This approach, successfully exploited in the past for producing hole transport layers for organic light emitting diodes (OLEDs),[40] also allows fabrication of organic cathodes with high cycling stability due to the insolubility of the cross-linked polymer network.[41] Our non-conjugated systems represent a unique platform for an in-depth understanding of the mixed ionic–electronic conduction mechanisms in non-conjugated organic redox materials.[42–45] Indeed, in non-conjugated **TPA**s, the electronic charge (hole) is naturally localized on a particular redox unit (**TPA**), avoiding an undefined degree of charge delocalization (*e.g.*, polaron) over the polymer backbone, as it may occur in π-conjugated systems, in which charge transport may thus follow a different transfer mechanism.[46,47] At the same time, charge localization allows electronic charge mobility by hopping, and cross-linked non-conjugated **TPA**-based polymers have been successfully exploited in the past for organic electronic applications.[38–40]

We introduce a novel procedure to model the microstructure of pristine and doped polymerized **TPA**s. For both cases, we compute the hole transport parameters, among which are the site energy differences and their time-dependent fluctuations. Our **TPA** systems show high static site energy disorder ($\sigma \sim 0.4$ eV) already in the pristine state. The energetic disorder increases in the presence of counter ions (hexafluorophosphate anions, PF_6^-), reaching σ values of up to ~ 1.70 eV. *Via* MD simulations, we demonstrate that the site energies undergo rapid fluctuations in time (ps-timescale) affecting the charge transfer rates. Such fast oscillations of the site energy landscape suggest that the use of a set of fixed charge transfer rates (*e.g.*, Marcus rates) for describing the electronic transport is not meaningful. Therefore, we devise a new approach to explicitly include the dynamics of disorder effects into the hole transport processes, namely to take into account the site energy

fluctuations as induced by the molecular vibrations, polymer chains and ion motions. We define an effective Marcus residence time of the charges on individual sites, considered as the average time required by a hole to escape from a trap. Distributions of charge escape times are derived, representing the hole de-trapping process governed by the interplay between the site energy fluctuations, polymer segments and ion movements. Linear polymers show more dense hole escape networks than cross-linked ones, suggesting a more efficient hole de-trapping developing as a function of time and disorder effects.

Polymerization and bulk morphology generation *via* MD simulations

At the basis of our computational investigation is the creation of reliable bulk morphologies *via* MD simulations. Details about the force field parametrization and the MD simulations are found in the ESI,† while a short overview is given here. Since the polymer structural parameters (*e.g.*, chain lengths, molecular weights, and morphology) are unknown experimentally we adopted a special *in silico* heuristic strategy, explored in the past to determine the morphology of cross-linked polymers.[48] A thermal annealing procedure was used to generate the equilibrated morphologies of the monomers (512 molecules per system) for both **TPA-1** and **TPA-2** species (*i.e.*, unreacted **TPA**s, showing intact oxetane rings (Fig. 1), see the ESI†). Afterwards, MD simulations coupled with the algorithm REACTER[49] (MD-REACTER) were performed to – heuristically – model the ring opening chemical reaction, which leads to the formation of polymers. It is important to mention that the CROP reaction shown in Fig. 2a leads to the formation of a cross-linked network (**xTPA**) in the case of two oxetane functionalities (**TPA-2**), while in the case of **TPA-1**, a linear polymer (**pTPA**) is formed. The initiation step was achieved by randomly placing 25 protons (and 25 chloride ions to ensure charge neutrality) in the monomer simulation boxes, corresponding to *ca.* 5 mol% initiator concentration, and running MD-REACTER simulations at high temperature (1000 K) and pressure (100 bar) to quickly reach complete oxetane conversion (*i.e.*, ring opening). Fig. 2b reports the CROP reaction turnover, showing a faster conversion of **TPA-1** compared to **TPA-2**. While experimentally, a yield of 100% is not achievable because of the limited diffusional mobility of the oxetane groups within the solid thin film, and in the simulation such a high turnover is possible under harsh thermodynamic conditions. Fig. 2c shows the chain length distribution for **pTPA** after 50 ps MD equilibration, and Fig. 2d (left panel) shows an exemplary MD box for the polymer. It should be noted here that the simulated polymer length distributions are limited by the system size of the simulations (*i.e.* 512 monomers) and cannot be directly compared to experimental values.

To better characterize the thermodynamic properties of the linear and cross-linked polymers, we computed the glass transition temperature (T_g) of both **pTPA** and **xTPA** (details in ESI†), by following the MD protocol reported by Lin *et al.* based on cooling the system from 800 K to 300 K and monitoring the density, followed by fitting of the linear regions in the

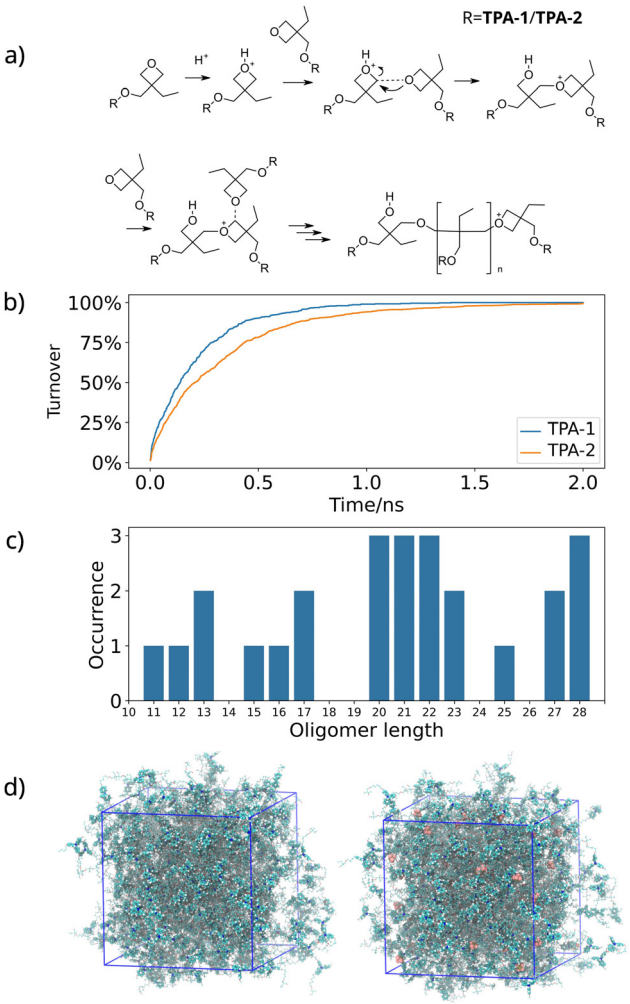

Fig. 2 (a) CROP mechanism.[40] (b)–(d) MD-REACTER simulations using 512 **TPA-1** or **TPA-2** monomers, respectively. (b) Oxetane ring opening turnover. (c) Oligomer length distribution after full oxetane conversion of **TPA-1**. (d) Simulation box for pristine cross-linked **xTPA** (left) and simulation box for **xTPA** with a 10% PF_6^- ion (brown structures) content (right).

density-temperature plots.[50] Depending on the choice of the fitting range, T_g was predicted to fall in the range between *ca.* 319–333 K (**pTPA**) and 308–328 K (**xTPA**), generally well matching the experimental data (see Fig. S5 in the ESI†) of 297 K (**pTPA**) and 325 K (**xTPA**). The procedure was not able to reproduce the experimental trend in the T_g for **pTPA** and **xTPA** (*i.e.* T_g (**xTPA**) > T_g (**pTPA**)); however, the computed T_g are overall acceptable. To strengthen our modeling approach, we experimentally determined the density of the monomeric systems and compared them to the simulated values, yielding good agreement and matching trends between **TPA-1** and **TPA-2** (see Table S16, ESI†). Furthermore, the T_g values of the 80% polymerized systems were determined, which are generally similar to the T_g values of the fully polymerized systems (see Fig. S9 and Tables S14, S15 in the ESI†). Therefore, the deviations of the simulated and experimental T_g are most likely due to the cooling protocol and force field parameters, rather than the polymer model or the polymerization degree.[51,52] We also

note here that the simulated T_g values lie above room temperature, in line with experimental data, meaning that all simulations were performed on solids. The polymer bulk morphologies of **pTPA** and **xTPA** correspond to that of the pristine case (*i.e.*, the absence of PF_6^-) and were used as the starting point for various production runs (*vide infra*).

The morphology and the bulk properties of the doped polymers were obtained by randomly inserting PF_6^- ions in the simulation box at various concentrations, and at the same time creating an equal number of positively charged **TPA** units. We considered different doping levels of 5%, 10% and 15% ion contents relative to the number of monomer units (an example of the MD simulation box at 10% doping is reported in Fig. 2d). For the charge transport analysis, after energy minimization and a further 50 ps MD run of thermal equilibration, both a 10 ps and a 100 ps MD trajectory were generated using sampling rates of one snapshot every 0.01 ps and 0.1 ps, respectively, to generate the data. For the ion diffusion, 300 ns MD trajectories of a singular PF_6^- ion in the bulk polymer morphologies were generated, following a similar procedure as reported by Webb *et al.*[53] The MD simulations were performed by using both LAMMPS[54] (coupled with MD-REACTER), for the generation of the polymerized bulk morphologies and for producing the trajectories for the charge transport analysis and GROMACS[55] (for the ion diffusion study). A reparametrized version of the OPLS-AA[56,57] force field was considered. For visualization and analysis, VMD[58] and TRAVIS[59] were adopted. The code HOLE[60] was used to characterise the dimensions and distribution of pores (voids) of the polymer bulk. Further details are reported in the ESI.† Restart files for all simulations can be found on Github under **https://github.com/rbrthrz/pTPA_xTPA**.

Charge transport parameters

Charge (hole) transport rates k_{ij} between two sites (*i.e.*, **TPA** units) i and j are computed using Marcus theory:[61,62]

$$k_{ij} = \frac{2\pi}{\hbar}\frac{J_{ij}^2}{\sqrt{4\pi\lambda k_B T}}\exp\left[-\frac{(\Delta E_{ij}+\lambda)^2}{4\lambda k_B T}\right] \quad (1)$$

For the evaluation of the charge transport parameters and rates, the open-source code VOTCA[63] was adopted. In eqn (1), ΔE_{ij} is the site energy difference, λ is the total reorganization energy and J_{ij} is the electronic coupling. J_{ij} is given by:[64]

$$J_{ij} = \langle \phi^i | \hat{H} | \phi^j \rangle \quad (2)$$

where $\phi^{i,j}$ are the highest occupied molecular orbitals (HOMOs) of sites i and j involved in the charge transfer reaction and $\hat{H}$ is the Hamiltonian operator of the dimer. In this work, J_{ij} is approximated with the molecular orbital overlap (MOO) method[65] based on ZINDO/S. The total reorganization energy λ consisting of an inner and an outer contribution is given by:

$$\lambda = \lambda_i + \lambda_o \quad (3)$$

Herein, reorganization energies calculated in a previous investigation[66] based on the adiabatic four point method[67] were used. For λ_o, an estimate of 0.05 eV was assumed, since the explicit calculation of the outer reorganization energy is computationally too demanding. The site energies E_i are given by:[63]

$$E_i = \frac{1}{4\pi\varepsilon_0}\sum_{a_i}\sum_{b_{k,k\neq i}}\frac{\left(q_{a_i}^c - q_{a_i}^n\right)q_{b_k}^n}{\varepsilon_s r_{a_i b_k}} \quad (4)$$

where q is the atomic partial charge, r is the distance, ε_0 is the vacuum dielectric constant and ε_s is dielectric constant of the material. The summation indices a and b run over the atoms of sites i and k, while the superscripts c and n indicate the electronic state (charge (+1), neutral). In this work, ε_s is given by 2.63 (**TPA-1**) and 2.64 (**TPA-2**), as computed from the Clausius–Mossotti eqn (5):

$$\varepsilon_s = 1 + \frac{12\pi\alpha\frac{N}{V}}{3 - 4\pi\alpha\frac{N}{V}} \quad (5)$$

In eqn (5), N is the number of molecules, V is the MD box volume, and α is the molecular polarizability as computed with VOTCA based on the atomic polarizabilities. The description of the site energies can possibly be improved by including distance-dependent screening or even explicit dipole–dipole interactions; however, this was not computationally feasible in the scope of this work. The atomic partial charges used for eqn (4) were calculated at the ωB97X-D[68] level with a triple-split polarized Pople basis set 6-311G*[69–71] and by employing the DDEC6 method, as implemented in the CHARGEMOL program.[72] The required geometry optimizations of **TPA-1** and **TPA-2** monomers were initially conducted *via* conformer searches using the semiempirical quantum mechanical (SQM) tight-binding DFT method GFN2-xTB[73] and CREST.[74] DFT calculations of neutral states were performed at the restricted level, while singly charged states (+1 oxidation state) were performed at the unrestricted spin-polarized level. All equilibrium optimized geometries were confirmed by frequency calculations. DFT and SQM calculations were performed with GAUSSIAN16[75] and xTB.[73] For the computation of the charge transport parameters in the charged cases, within VOTCA the **TPA**-units closest to the PF_6^- ions were set to the monocationic state to balance out the negative charge of the counterions. In this way, the presence of the counterions affects the charge transport by impacting the site energies through their atomic partial charges.

Bulk structural analysis

The bulk morphologies of the monomeric materials (*i.e.*, **TPA-1** and **TPA-2**, before the ring-opening polymerisation) and polymers (*i.e.*, **pTPA** and **xTPA**) were analysed with regard to their structural features. Fig. 3a compares the radial distribution function of the nitrogen centers, $g_{NN}(r)$, which are representative of amorphous morphologies, being unstructured at long range distances. In the case of **xTPA,** a slightly less featured band is observed compared to **TPA-2**, which is related to the more rigid cross-linked network, hindering local ordering of

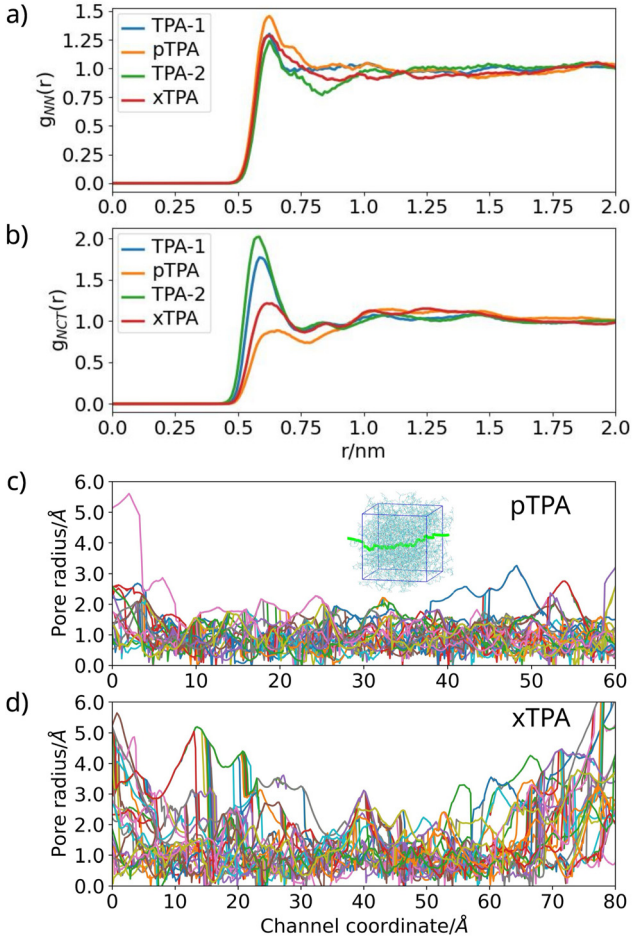

Fig. 3 Radial distribution functions of (a) the nitrogen-centers ($g_{NN}(r)$) and (b) the nitrogen-centers with respect to the tertiary oxetane carbon ($g_{NCT}(r)$) in **TPA-1**/**pTPA** (blue/orange) and **TPA-2**/**xTPA** (green/red) systems. Panels (c) and (d) show the overlayed pore radii across the MD box for different trajectories for the polymerized bulk morphologies of **pTPA** and **xTPA**. Different colours represent different trajectories probing the pore size across the simulation box. In light green, an exemplary trajectory across the simulation box is shown (inset).

the repeat units. Interestingly, the nitrogen–nitrogen distances are quite similar for all materials.

In Fig. 3b, the radial distribution function of the nitrogen-centers and the tertiary oxetane carbons $g_{NCT}(r)$ show a drastic change upon cross-linking. The first band shows as expected a strong decrease upon polymerization. While in the monomeric phase the **TPA** redox-units can assume a coiled conformation, where the oxetane units and the nitrogen-centers can be in close contact, such conformational freedom is not given in polymers. In the latter, the former oxetane units constitute the polymer backbone and their mobility is therefore hindered, limiting coiled configurations and close contact with the nitrogen centers.

Since monomeric (unreacted) **TPA-1** and **TPA-2** cannot be used for OMIECs and battery applications due to their solubility in the electrolyte, both were not included in the following investigations. Fig. 3c and d show the radii of the pores inside the **xTPA** and **pTPA** bulk, respectively. The overlayed void radii were computed with the code HOLE, by using 100 probing trajectories across the bulk of the polymers. Stronger variations in pore radii are encountered in **xTPA** than in **pTPA**, due to the more bundled structure of the polymer network formed by the two-armed system. The void radii vary generally below 2–4 Å in both cases. Such pore radii are of similar magnitude compared to the ion radius of PF_6^- (2.33–2.88 Å[76]). The overall average pore radius for all probing trajectories in **pTPA** is 1.69 Å, while for **xTPA** it is 1.83 Å. This structural feature suggests a generally slow ion diffusion process throughout the materials, as it will be evaluated *via* the MD simulations in the next section.

Ion transport

The PF_6^- ion transport is quantified by analysing the MD trajectory of the ion inserted in the polymer bulk phases.[77,78] The mean square displacement (MSD) of the PF_6^- ion positions is about one order of magnitude less in **xTPA** than in **pTPA** (see Fig. 4). In long MD trajectories, even after 100 ns, the ion transport has not become diffusive yet (*i.e.*, MSD $\sim t$), as shown by the significant deviation of the MSD gradient from unity. The computed ion transport is rather in a sub-diffusive regime (*i.e.*, MSD $\sim t^{0.5}$), implying that during the timescale considered for hole transport (100 ps, *vide infra*), only very short distances are covered by the PF_6^- ions. Sub-diffusive regimes have been well documented in the literature of ion transport in polymer electrolytes.[53,77] Despite the limited displacements of ions, due to strong electrostatic effects even small ion movements can have a significant influence on the site energy differences (ΔE_{ij}) and their time-dependent fluctuations ($\Delta E_{ij}(t)$) (*vide infra*).

Static site energy landscape in pTPA and xTPA polymers

In a first assessment of the hole transport properties, the site energy landscape was investigated. It is commonly accepted

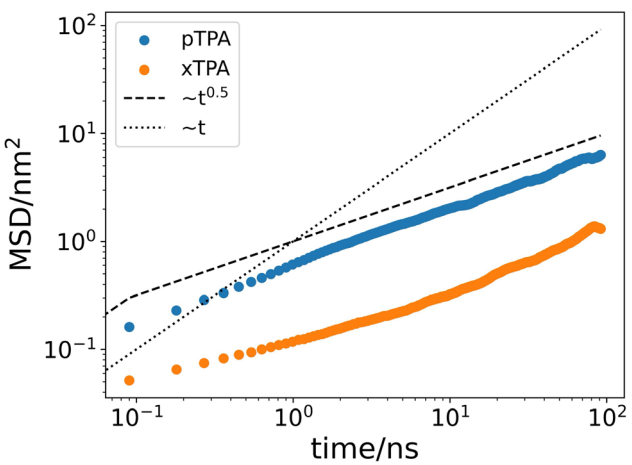

Fig. 4 Log–log plot of the mean square displacement (MSD) of a single PF_6^- ion in **pTPA** (blue) and **xTPA** (orange) bulk phases *vs.* time, as obtained *via* MD simulations. The dotted line shows the linear (diffusive) regime (*i.e.*, MSD $\sim t$), while the dashed line shows the sub-diffusive one (*i.e.*, MSD $\sim t^{0.5}$).

that high energetic disorder (high ΔE_{ij}) leads to charge trapping and low hole transfer rates (see eqn (1)). The static site-energy difference distributions for pristine and doped **pTPA** and **xTPA** are shown in Fig. 5.

High energetic disorder is already present in the undoped (pristine) cases, (σ = 0.37 eV) due to the high conformational disorder (amorphous phases, see the radial distribution functions given in Fig. 3a and b) of the alkyl linkers, combined also with remarkable electrostatic effects as provided by the oxygen atoms of the polymer chains. When the doping level increases (from 5% to 15% doping), the energetic disorder becomes larger due to electrostatic effects provided by the presence of the counterions (PF_6^-). Such high static disorder, with computed σ values ranging from 0.87 eV to 1.67 eV, is usually indicative of non-conductive materials and deep intrinsic traps for the electronic charges (tail states). For comparison, an MD simulated amorphous film of **TPA** monomers without oxetane chains is characterized by a σ value of 0.18 eV, leading to a computed hole mobility of 2.5×10^{-2} cm^2 V^{-1} s^{-1}.[66] In Monte–Carlo simulations based on the Gaussian disorder model, σ values of about 0.1 eV are often reported based on experimental observations.[79–81] However, as anticipated in the Introduction section, the time-dependent oscillations of the site-energies in the presence of alkyl groups and/or ions become crucial for understanding the coupled electronic–ionic transfer in OMIECs, being the key for allowing the energy level alignment[33] thus opening effective charge transport channels, as it will be discussed in the following section.

Dynamics of disorder in pTPA and xTPA polymers

To assess the dynamics of disorder effects, the site energy differences were evaluated over a time of 100 ps (10^3 frames, one snapshot every 100 fs), as shown in Fig. 6a. Large fluctuations can be observed in both cases. This finding prompted us to perform a deeper analysis to quantify the dynamics of disorder by calculating the time autocorrelation function (ACF) of the site energy differences, which is given by:

$$\mathrm{ACF} = \langle \Delta E_{ij}(t_0) \Delta E_{ij}(t_0 + \tau) \rangle \quad (6)$$

where t_0 is the starting time and τ is the time-lags. Here, a 10 ps MD trajectory (one snapshot every 10 fs) was used, and the ACF was averaged over 20 close-contact **TPA**-pairs. Furthermore, a running average over 10 timestep (100 fs) at a time was performed to filter out high frequency vibrations that are not well-described by classical MD.

As reported in Fig. 6b and c, the ACF quickly decays to zero – in about 1 ps – for all cases, followed by slower fluctuations that start to emerge on longer timescales. The dynamics underlying this behaviour are characterised by various processes occurring at different timescales, such as fast processes, as induced by bond vibrations (*e.g.*, C–C stretching occurring at 20–40 ps^{-1}), and slow processes, as given by the polymer segment rearrangements and ion motions. Additional fitting of the ACFs with an exponential function was performed and the data are reported in the ESI† (Fig. S10 and S11). For both **pTPA** and

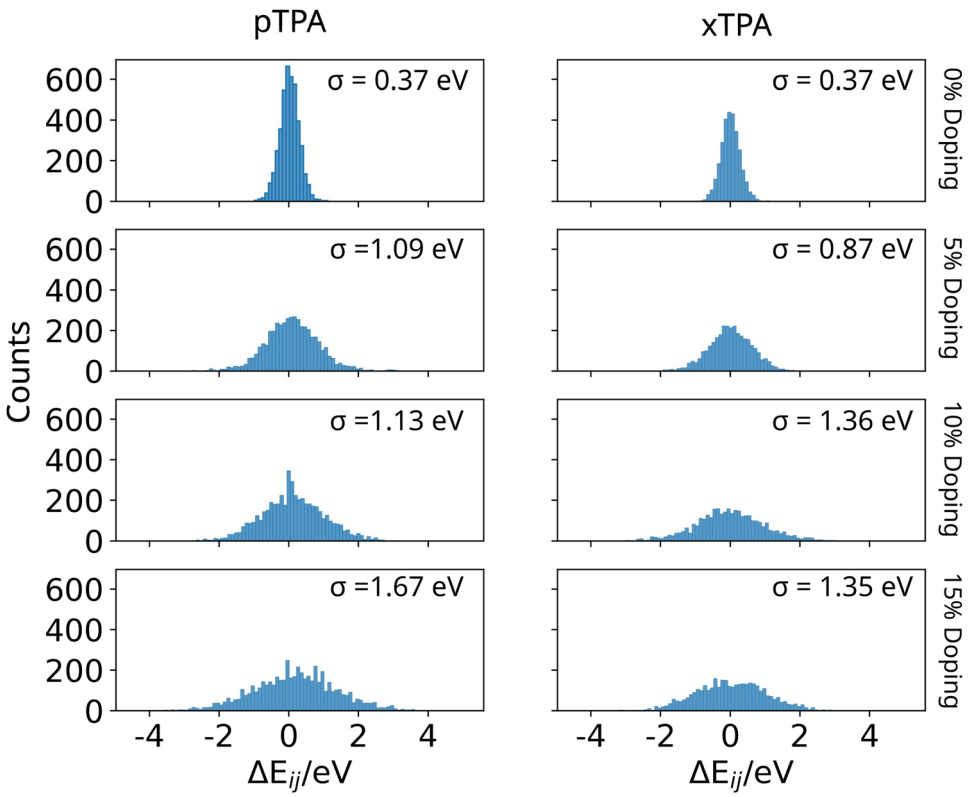

Fig. 5 Site energy difference (ΔE_{ij}) distributions of **pTPA** (left) and **xTPA** (right) polymers with 0%, 5%, 10% and 15% (top to bottom) PF_6^- ion contents (doping level), respectively. The computed σ values are given as insets.

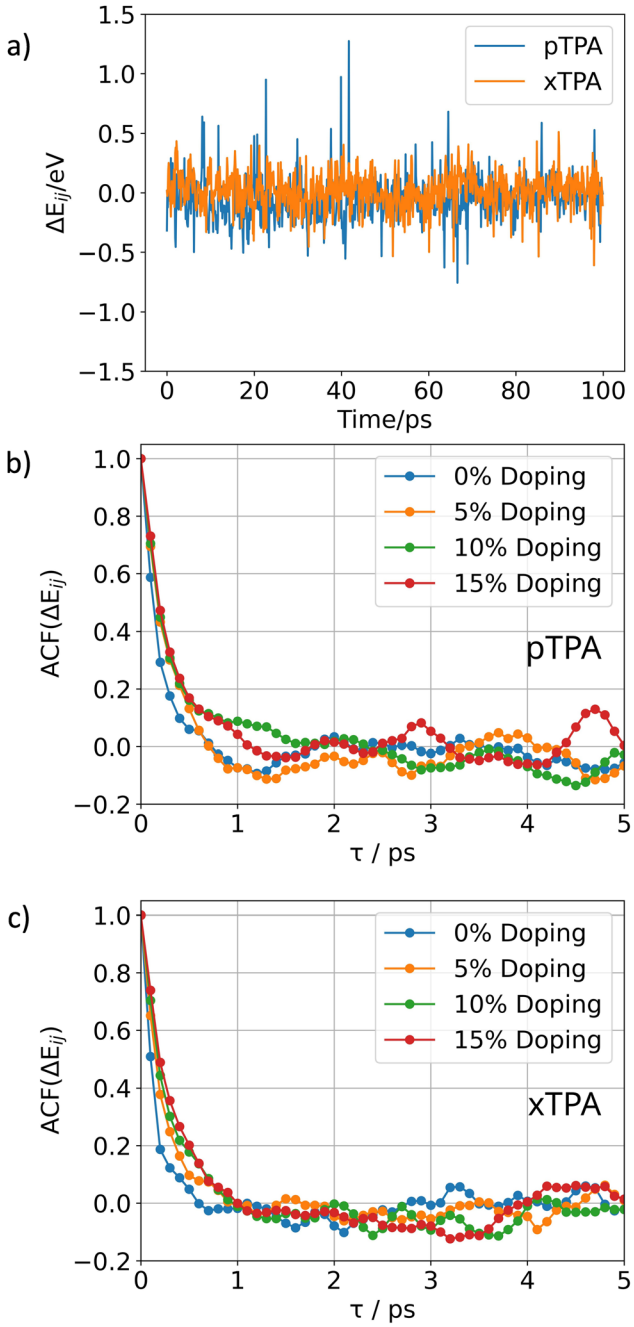

Fig. 6 (a) Site energy difference (ΔE_{ij}) fluctuations of a sample pair in pristine (= undoped) **pTPA** (blue) and **xTPA** (orange). Autocorrelation functions (ACF) of the site energy differences for the pristine (0% doping – blue) and doped (5% – orange, 10% – green and 15% – red, doping levels) cases for (b) **pTPA** and (c) **xTPA**.

xTPA, the pristine case (0% doping) shows a decay time constant ranging from 140 to 180 fs. By increasing the doping level, the time constants increase up to *ca.* 300 fs. Such decay times may be related to low-intermolecular vibrational modes (below 100 cm^{-1}) and for the case of doped systems, to the coupling modes between polymer segments and ions. The large fluctuations of the site energies lead to a temporally changing distribution of Marcus transfer rates spanning over orders of

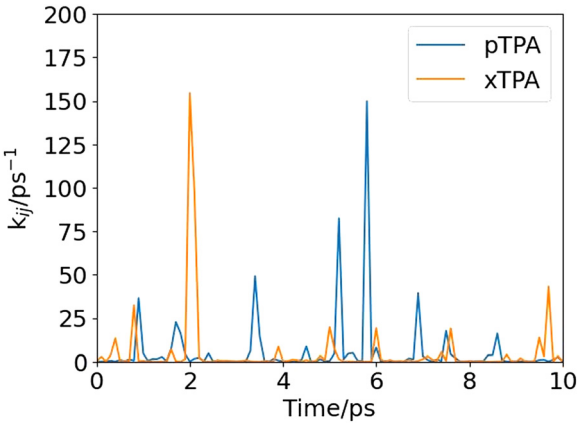

Fig. 7 Computed Marcus hole transfer rates (eqn (1)) for a sample pair as taken from the pristine **pTPA** (blue) and **xTPA** (orange) morphology over a time of 10 ps.

magnitudes (see Fig. 7), which complicate the analysis of the charge transport.

In a system characterised by such strongly fluctuating rates over a short period of time (~10 ps), charge transfer channels open and close quickly and continuously. Therefore, the standard approach of using kinetic Monte Carlo and state-to-state dynamics with a fixed set of rates (k_{ij}) is no longer applicable, because the assumption of a timescale separation of the site energy-fluctuations and the charge transfer events is *de facto* not present. The dynamics of the system become the determining factor influencing the hole transport, which has been conceptualized as a highly interdependent, coupled phenomenon. Due to the high dynamic disorder, the electronic charges (holes) can reside on a site until a favourable energy level alignment occurs and the transfer event can take place.

Effective Marcus residence times

Due to the large fluctuations of the site energy differences, leading to time-dependent transfer rates, a new approach is needed to analyse the electronic transport by taking into account high energetic disorder effects, as well as the polymer segments and ion oscillations. We replace the instantaneous hopping rates (k_{ij}) with the half-time of hopping between sites i and j by integrating the time-dependent $k_{ij}(t)$ over a period of time. For an (i, j) pair, with a time dependent rate $k_{ij}(t)$, we compute the hypothetical time evolution of the charge population ($P_i(t)$) due to hopping from site i to site j (assuming that only the hopping $i \rightarrow j$ can take place). The time-dependent charge population $P_i(t)$ of site i reads as follows:[82]

$$-\frac{dP_i(t)}{dt} = k_{ij}(t)e^{-k_{ij}(t)t} \quad (7)$$

Rearranging and integrating yields:

$$P_i(T) = P_i(0) - \int_0^T k_{ij}(t)e^{-k_{ij}(t)t}dt \quad (8)$$

where T is the total integration time. The integral on the right-hand side of eqn (8) can be numerically solved by discretizing

the total integration time T in N discrete intervals ΔT. Assuming the charge on site i, that is $P_i(0) = 1$, the final expression for the population of site i, $P_i(T)$ reads as follows:

$$P_i(T = N\Delta T) = 1 - \sum_{n=1}^{N} k_{ij}(t_n) e^{-k_{ij}(t_n)t_n} \Delta T \quad (9)$$

We compute $P_i(T)$ for all triphenylamine pairs of **pTPA** and **xTPA** bulk systems over an integration time (T) of 100 ps, by using a sampling rate of one snapshot every 100 fs, thus resulting in a ΔT of 0.1 ps. We term the half-time of the population decay as the effective Marcus residence time $\tau_{i\to j}$. In the ESI,† an example for the $P_i(T)$ decay is reported. $\tau_{i\to j}$ represents a new descriptor for the electronic charge transport, considering the time-dependent history of the sites and encompassing the intrinsic dynamics of the systems. It can be used to quantify the influence of the dynamics of disorder, going beyond the static picture provided by the Marcus rates k_{ij}.

We calculate the distributions of lifetimes (t_i),[83] defined as the time required by a hole to escape from a given site i to any possible site j. t_i can be computed by considering either the static, instantaneous Marcus rates (k_{ij}, eqn (1)) or the effective Marcus residence times $\tau_{i\to j}$. If t_i is evaluated based on static rates, the lifetime of a carrier is given by:

$$t_i^{\text{static}} = \left(\frac{1}{\sum_j k_{ij}} \right) \quad (10)$$

while if it is based on the effective Marcus residence times $\tau_{i\to j}$ it reads:

$$t_i^{\text{effective}} = \left(\sum_j \frac{1}{\tau_{i\to j}} \right)^{-1} \quad (11)$$

Fig. 8 reports the distributions of lifetimes t_i of a hole for both **pTPA** and **xTPA** in the pristine case and at different doping states (5%, 10% and 15% of PF_6^-). The distribution of $t_i^{\text{effective}}$ is narrower for all cases (pristine and doped states) than those obtained from t_i^{static}, and the latter being more equally distributed. Note that many t_i^{static} are computed at longer time, outside the range considered in the figure, while no effective lifetime is longer than 100 ps, *i.e.* the main effect of including the dynamic disorder is to remove long-lived trap states. While there are no prominent differences between **pTPA** and **xTPA** in the distributions of lifetimes, some variations can be observed by comparing pristine with respect to doped states. The presence of counterions (5% to 15% of PF_6^-) does not hinder the charge transfer events (or, equivalently, the de-trapping of

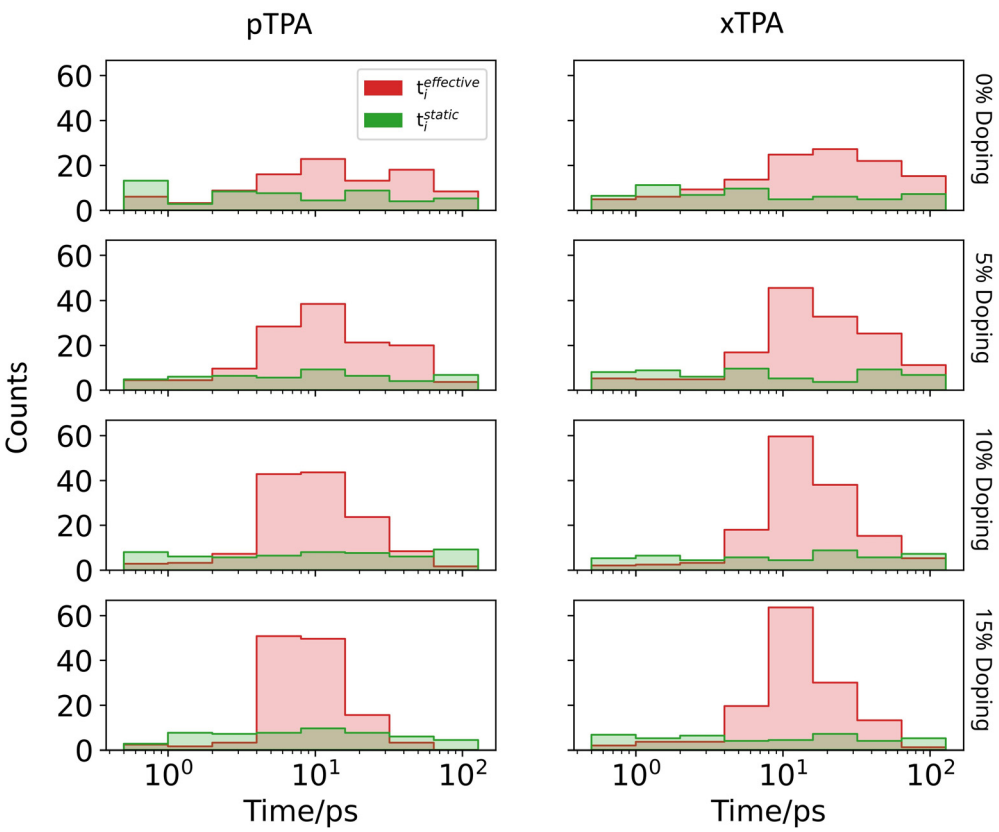

Fig. 8 Distributions of static (t_i^{static}, green) and effective ($t_i^{\text{effective}}$, red) lifetimes for **pTPA** (left) and **xTPA** (right) from pristine (0% doping, top panels) to 5%, 10% and 15% doping (lower panels).

electronic charges) despite the high static disorder (see Fig. 5). Instead, it narrows the lifetime distributions, as evident by moving from 5% to 15% doping (see Fig. 8). Comparing doped **pTPA** and **xTPA** we can further understand the role of the polymer structure. The PF_6^- ions were found to be more mobile in **pTPA** than in **xTPA**, as shown by their higher diffusion (see Fig. 4). This leads to a larger accumulation of shorter $t_i^{\text{effective}}$ in **pTPA** compared to **xTPA**, and thus a more efficient trap removal in linear than cross-linked polymers.

To gain further atomistic insights into the coupled hole and ionic transport, we report the three-dimensional networks of the effective Marcus residence times ($\tau_{i\to j}$) in Fig. 9a and their two-dimensional graph representations in Fig. 9b. We call these visualization hole transport networks and they should not be confused with the (cross-linked) polymer network, as mentioned in the Structural analysis section. Hole transport networks are a convenient representation to understand the topological aspects of the charge transport, and we point the reader to a series of publications where such representations have been introduced and explained in details.[84–88] Each point (node) in these representations constitutes a **TPA** site, and each line (edge) represents an effective Marcus residence time $\tau_{i\to j}$ connecting two sites. Connections between sites represent both a spatial and a time-dependent information: the spatial information concerns which **TPA** sites are involved in the hole transfer process, while the time information regards how much time it takes for a hole to be released from a deep trap. Red lines in Fig. 9a and b represent short $\tau_{i\to j}$, that is depopulation of trap states at early time (0.1 to 1 ps), resulting in a rapid hole transfer process from site i to j despite the high static energetic disorder. Green and blue lines

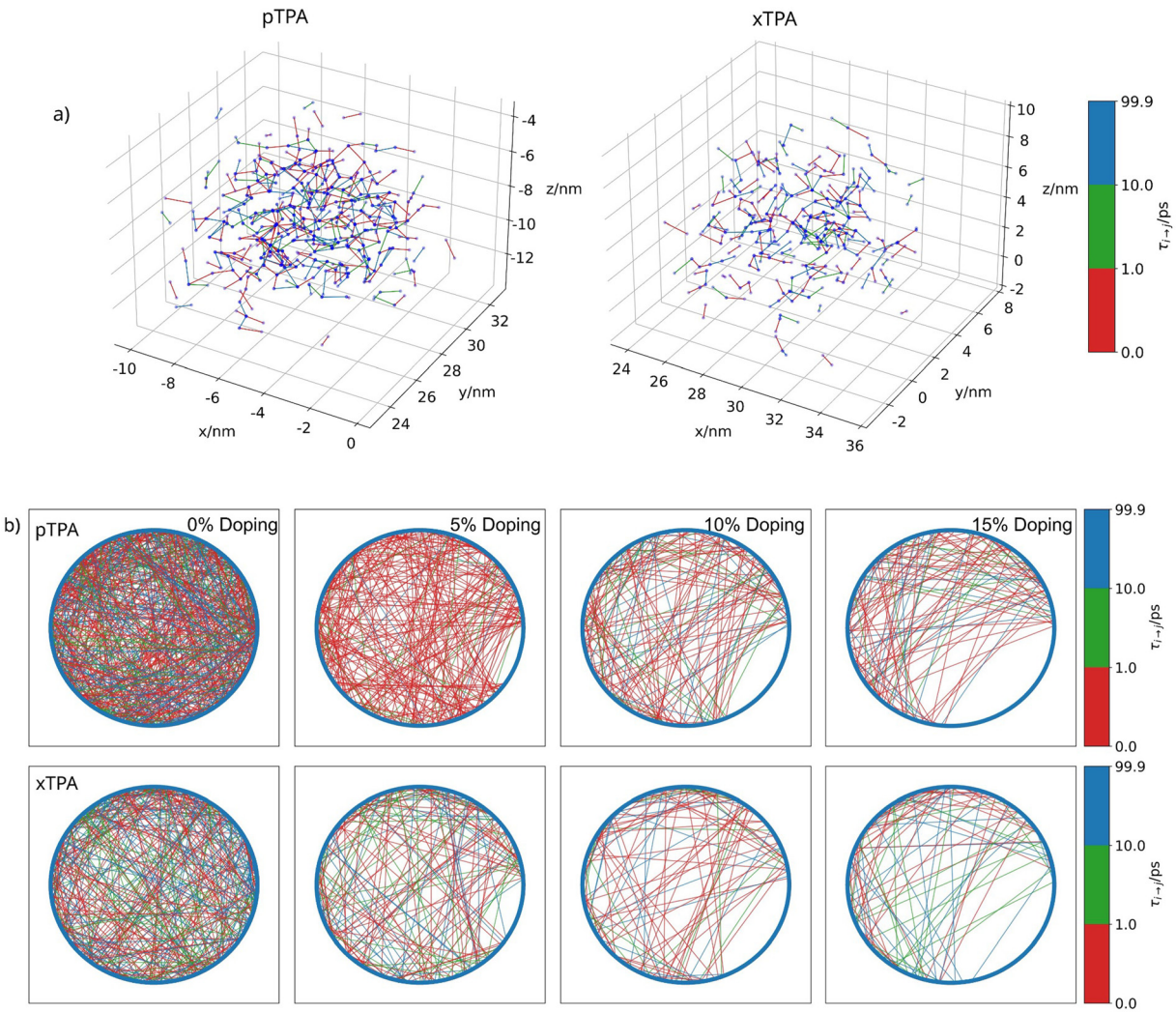

Fig. 9 3D (top) and 2D (bottom) representations of the hole transport networks. (a) Real space representation: nodes are **TPA** units (positioned in real space, *i.e.*, simulation box), while edges (connections between nodes) are effective Marcus residence times $\tau_{i\to j}$ for the pristine case (0% doping) of **pTPA** (left) and **xTPA** (right). A distance cut-off of 6 nm between sites is used to exclude edges crossing the periodic boundary conditions from the plot. (b) 2D representations: nodes are **TPA** units reported as a circular graph, and edges are effective Marcus residence times $\tau_{i\to j}$ computed for 0%, 5%, 10% and 15% doping cases (**pTPA**, top row, and **xTPA**, bottom row). Non-connected nodes have not developed a transfer event within 100 ps or are **TPA** units with fixed positive charges as counterions to the PF_6^- ions that do not take part in the charge transport. Unlike in (a) no cut-off is employed (*i.e.* a full network is shown).

show the same process, however on a longer time scale (up to $\tau_{i\rightarrow j}$ = 99.9 ps). Detrapping events taking only place after more than 100 ps (*i.e.* $\tau_{i\rightarrow j}$ = 100 ps) are not shown.

In Fig. 9a, we compare pristine **pTPA** (left) and **xTPA** (right), in real space (*i.e.*, MD simulation boxes). Fig. 9b reports the same hole transport networks; however, in an abstract form, that is a circular 2D representation in which the morphological information is removed to better focus on the overall density (*i.e.*, number of lines per area) or connectivity of the hole transport network. Both in the pristine (0%) and in the doped cases (5%, 10%, and 15%), **pTPA** shows a denser hole transport network than **xTPA**, indicating more efficient trap removal (*i.e.*, hole de-trapping events) which can be traced back to a higher ion mobility (Fig. 4) and a lower bulk structural porosity (Fig. 3c and d). The addition of counterions reduces the density of the hole transport network. Such reduction decreases the de-trapping events thus impacting the hole bulk transport which lowers as moving from 5% up to 15% doping. **xTPA** shows hole transport networks which are less dense than that of **pTPA**, reflecting a less efficient trap removal, meaning slower hole de-trapping dynamics (as shown by the green and blue lines in Fig. 9b).

Our analysis captures the fine balance between the dynamics of the trap removal and the dynamics of disorder effects. We stress here that a dynamical approach is essential to understand the complex and coupled ionic–electronic transport motions. Possible charge transport pairs that are not electronically connected initially (*i.e.*, vanishing static k_{ij}, eqn (1)) can instead develop at a later stage a high hole transfer rate through the fluctuations of the system (leading to a decrease of residence time $\tau_{i\rightarrow j}$). At the same time, pairs that are connected initially can become disconnected over time. Developing a charge transport analysis which does not consider the time dependency of the transfer rates as well as the density of the hole transport network between all pairs might lead to erroneous conclusions about the physics of the charge transport in highly disordered soft materials.

Conclusions

The coupled electronic and ionic transport in linear (**pTPA**) and cross-linked (**xTPA**) triphenylamine based non-conjugated redox polymers was investigated using a bottom-up multiscale computational approach. The investigated systems are ideal for studying this phenomenon since they feature localized electronic charges (holes), thus legitimizing the evaluation of the charge transfer rates *via* Marcus theory. Polymer chains and bulk formation were modelled by interfacing a heuristic protocol together with extended MD simulations to obtain realistic bulk structures. Morphologies of linear and cross-linked **TPA** polymers show disordered, amorphous structures with short-range coordination between the nearest neighbour redox units. The internal porosity of the polymer films was analysed, yielding larger pore radius variations in cross-linked **xTPA** compared to linear **pTPA** polymers. Insertion of PF_6^- ions was modelled at different doping concentrations, namely 5%, 10% and 15%. Doping causes only minor variations in the polymer bulk morphologies. Energetic disorder effects (site energy differences) were explicitly computed in the static limit leading to broad distributions for both pristine (0.37 eV) and doped polymers, by increasing the ion content up to 1.67 eV. Such large static energetic disorder would hinder any hole transfer process, challenging the experimentally observed electronic and ionic conduction. Dynamic effects are the key to explain the hole release from deep trap states. We computed the dynamics, *i.e.* the time-dependent fluctuations of the site energy differences of pristine and doped polymers, together with their autocorrelation functions. The timescales characterising the decay of the site energy autocorrelation function were found to be around 1 ps, leading to fast and large fluctuations of the hole Marcus transfer rates, opening and closing electronic charge transfer pathways continuously. The dynamics of disorder effects impact the electronic couplings as well, inducing fast fluctuations generally ranging in the order of the fs time-scales. Here, we focused on the analysis of the site energy fluctuations, as they represent the rate-limiting factor since their oscillations and correlation function decay on slower timescales than the electronic couplings. To include the time-dependent disorder effects in a unified electronic transport description, we introduced for the first time an effective Marcus residence time $\tau_{i\rightarrow j}$, which considers the temporal history of disorder effects. From $\tau_{i\rightarrow j}$, we estimate for each polymer and for both pristine and doped states, distributions of lifetimes, defined as the time required by a hole to escape from a deep trap. We observed that the dynamics of disorder effects can lead to efficient de-trapping and formation of hopping hole transport networks within the polymer bulk. Our study shows the complex and entangled nature of mixed charge- and ion transport in non-conjugated redox soft materials of potential use for organic electrodes. Hole transport cannot be modelled and rationalised in an isolated manner, but has to be analysed considering the spatial and time-dependent interaction between polymer chains, ions and electronic charge carriers.

Author contributions

R. H.: simulations, data curation, conceptualization, and manuscript writing. L. P.: experimental data, T_g and density determination. A. T.: conceptualization and manuscript writing. K. M.: conceptualization and manuscript writing. D. F.: conceptualization, data curation, and manuscript writing.

Conflicts of interest

The authors declare no conflicts of interest.

Data availability

The data supporting this article have been included as part of the ESI.† Technical data (*e.g.*, restart files for all simulations)

can be found on Github under **https://github.com/rbrthrz/pTPA_xTPA**.

Acknowledgements

R. H., L. P., D. F. and K. M. acknowledge the DFG Research Training Group 2591 ''Template-designed Organic Electronics (TIDE)'' for supporting their research. They also acknowledge the Regional Computing Centre (RRZK) of the University of Cologne for providing computing time and resources on the HPC RRZK CHEOPS. K. M. acknowledges the DFG Priority Programme ''Polymer Based Batteries'' (SPP 2248) with the grant ''SYNERGISTIC'' (ME1246-43). D. F. acknowledges the Global Faculty Program of the University of Cologne within the focus area ''Quantum Matter and Materials (QM2)'', the National Recovery and Resilience Plan (NRRP), the Mission 04 Component 2 Investment 1.5 – NextGenerationEU, Call for tender no. 3277 dated 30/12/2021, Award Number: 0001052 dated 23/06/2022, and the National Project funded by the European Union – Next Generation EU, Project title ''Modelling and design of organic conjugated redox materials for energy-saving applications: a bottom-up strategy'', code MUR 2022 WKTH9E – CUP J53D23008810006. A. T. acknowledges the support from the European Research Council (grant no. 101020369).

References

‡ In this work, the terms doping level and charging level both refer to the number of positively charged **TPA** units and an equal number of PF_6^- counterions, and can be used interchangeably.

1 P. Gkoupidenis, Y. Zhang, H. Kleemann, H. Ling, F. Santoro, S. Fabiano, A. Salleo and Y. van de Burgt, *Nat. Rev. Mater.*, 2024, **9**, 134–149.
2 B. D. Paulsen, K. Tybrandt, E. Stavrinidou and J. Rivnay, *Nat. Mater.*, 2020, **19**, 13–26.
3 J. Rivnay, S. Inal, A. Salleo, R. M. Owens, M. Berggren and G. G. Malliaras, *Nat. Rev. Mater.*, 2018, **3**, 1–14.
4 S. Fabiano, L. Flagg, T. C. Hidalgo Castillo, S. Inal, L. G. Kaake, L. V. Kayser, S. T. Keene, S. Ludwigs, C. Muller, B. M. Savoie, B. Lüssem, J. L. Lutkenhaus, M. Matta, D. Meli, S. N. Patel, B. D. Paulsen, J. Rivnay and J. Surgailis, *J. Mater. Chem. C*, 2023, **11**, 14527–14539.
5 S. Kang, J. Fan, J. B. P. Soares and M. Gupta, *RSC Adv.*, 2023, **13**, 5096–5106.
6 C. J. Kousseff, R. Halaksa, Z. S. Parr and C. B. Nielsen, *Chem. Rev.*, 2022, **122**, 4397–4419.
7 S. Yu, H.-Y. Wu, V. Lemaur, C. J. Kousseff, D. Beljonne, S. Fabiano and C. B. Nielsen, *Angew. Chem.*, 2024, **136**, e202410626.
8 N. A. Kukhta, A. Marks and C. K. Luscombe, *Chem. Rev.*, 2022, **122**, 4325–4355.
9 D. Moia, A. Giovannitti, A. A. Szumska, I. P. Maria, E. Rezasoltani, M. Sachs, M. Schnurr, P. R. F. Barnes, I. McCulloch and J. Nelson, *Energy Environ. Sci.*, 2019, **12**, 1349–1357.
10 Y. Wang, S. Wustoni, J. Surgailis, Y. Zhong, A. Koklu and S. Inal, *Nat. Rev. Mater.*, 2024, **9**, 249–265.
11 C. B. Nielsen, A. Giovannitti, D.-T. Sbircea, E. Bandiello, M. R. Niazi, D. A. Hanifi, M. Sessolo, A. Amassian, G. G. Malliaras, J. Rivnay and I. McCulloch, *J. Am. Chem. Soc.*, 2016, **138**, 10252–10259.
12 A. Giovannitti, D.-T. Sbircea, S. Inal, C. B. Nielsen, E. Bandiello, D. A. Hanifi, M. Sessolo, G. G. Malliaras, I. McCulloch and J. Rivnay, *Proc. Natl. Acad. Sci. U. S. A.*, 2016, **113**, 12017–12022.
13 R. Kroon, D. Kiefer, D. Stegerer, L. Yu, M. Sommer and C. Müller, *Adv. Mater.*, 2017, **29**, 1700930.
14 I. Yu, D. Jeon, B. Boudouris and Y. Joo, *Macromolecules*, 2020, **53**, 4435–4441.
15 S. Muench, A. Wild, C. Friebe, B. Häupler, T. Janoschka and U. S. Schubert, *Chem. Rev.*, 2016, **116**, 9438–9484.
16 Y. Chen and C. Wang, *Acc. Chem. Res.*, 2020, **53**, 2636–2647.
17 J. Kim, Y. Kim, J. Yoo, G. Kwon, Y. Ko and K. Kang, *Nat. Rev. Mater.*, 2023, **8**, 54–70.
18 T. B. Schon, B. T. McAllister, P.-F. Li and D. S. Seferos, *Chem. Soc. Rev.*, 2016, **45**, 6345–6404.
19 P. Poizot, J. Gaubicher, S. Renault, L. Dubois, Y. Liang and Y. Yao, *Chem. Rev.*, 2020, **120**, 6490–6557.
20 K. A. Ludwig, J. D. Uram, J. Yang, D. C. Martin and D. R. Kipke, *J. Neural Eng.*, 2006, **3**, 59–70.
21 Q. Pei, G. Yu, C. Zhang, Y. Yang and A. J. Heeger, *Science*, 1995, **269**, 1086–1088.
22 J. Jang, J. Ha and J. Cho, *Adv. Mater.*, 2007, **19**, 1772–1775.
23 M. Winter, B. Barnett and K. Xu, *Chem. Rev.*, 2018, **118**, 11433–11456.
24 M. S. Whittingham, *Chem. Rev.*, 2014, **114**, 11414–11443.
25 C. Friebe, A. Lex-Balducci and U. S. Schubert, *ChemSusChem*, 2019, **12**, 4093–4115.
26 N. Siemons, D. Pearce, C. Cendra, H. Yu, S. M. Tuladhar, R. K. Hallani, R. Sheelamanthula, G. S. LeCroy, L. Siemons, A. J. P. White, I. McCulloch, A. Salleo, J. M. Frost, A. Giovannitti and J. Nelson, *Adv. Mater.*, 2022, **34**, e2204258.
27 S. T. Keene, V. Gueskine, M. Berggren, G. G. Malliaras, K. Tybrandt and I. Zozoulenko, *Phys. Chem. Chem. Phys.*, 2022, **24**, 19144–19163.
28 S. T. Keene, J. E. M. Laulainen, R. Pandya, M. Moser, C. Schnedermann, P. A. Midgley, I. McCulloch, A. Rao and G. G. Malliaras, *Nat. Mater.*, 2023, **22**, 1121–1127.
29 S. Sunny, S. Shah, M. Garg, I. Zozoulenko and S. Ghosh, *Macromolecules*, 2024, **57**, 5155–5165.
30 A. Khot and B. M. Savoie, *J. Polym. Sci.*, 2022, **60**, 610–620.
31 A. Giovannitti, I. P. Maria, D. Hanifi, M. J. Donahue, D. Bryant, K. J. Barth, B. E. Makdah, A. Savva, D. Moia, M. Zetek, P. R. F. Barnes, O. G. Reid, S. Inal, G. Rumbles, G. G. Malliaras, J. Nelson, J. Rivnay and I. McCulloch, *Chem. Mater.*, 2018, **30**, 2945–2953.
32 Y. Tsarfati, K. C. Bustillo, B. H. Savitzky, L. Balhorn, T. J. Quill, A. Marks, J. Donohue, S. E. Zeltmann, C. J. Takacs, A. Giovannitti, I. McCulloch, C. Ophus, A. M. Minor and A. Salleo, *Nat. Mater.*, 2025, **24**, 101–108.

33 C. Burke, A. Landi and A. Troisi, *Mater. Horiz.*, 2024, **11**, 5313–5319.
34 A. Landi, M. Reisjalali, J. D. Elliott, M. Matta, P. Carbone and A. Troisi, *J. Mater. Chem. C*, 2023, **11**, 8062–8073.
35 S. D. Baranovskii, *Phys. Status Solidi B*, 2014, **251**, 487–525.
36 S. D. Baranovskii, *Phys. Status Solidi A*, 2018, **215**, 1700676.
37 S. Inal, G. G. Malliaras and J. Rivnay, *Nat. Commun.*, 2017, **8**, 1767.
38 E. Bacher, M. Bayerl, P. Rudati, N. Reckefuss, C. D. Müller, K. Meerholz and O. Nuyken, *Macromolecules*, 2005, **38**, 1640–1647.
39 S. Jungermann, N. Riegel, D. Müller, K. Meerholz and O. Nuyken, *Macromolecules*, 2006, **39**, 8911–8919.
40 S. Feser and K. Meerholz, *Chem. Mater.*, 2011, **23**, 5001–5005.
41 L. Plein, L. Höfer, R. Herzhoff, D. Fazzi and K. Meerholz, *In Preparation*.
42 K. Yamamoto, D. Suemasa, K. Masuda, K. Aita and T. Endo, *ACS Appl. Mater. Interfaces*, 2018, **10**, 6346–6353.
43 L. Fan, Q. Liu, Z. Xu and B. Lu, *ACS Energy Lett.*, 2017, **2**, 1614–1620.
44 F. A. Obrezkov, A. F. Shestakov, V. F. Traven, K. J. Stevenson and P. A. Troshin, *J. Mater. Chem. A*, 2019, **7**, 11430–11437.
45 J. K. Feng, Y. L. Cao, X. P. Ai and H. X. Yang, *J. Power Sources*, 2008, **177**, 199–204.
46 D. Fazzi, S. Fabiano, T.-P. Ruoko, K. Meerholz and F. Negri, *J. Mater. Chem. C*, 2019, **7**, 12876–12885.
47 G. LeCroy, R. Ghosh, V. Untilova, L. Guio, K. H. Stone, M. Brinkmann, C. Luscombe, F. C. Spano and A. Salleo, *Mater. Horiz.*, 2024, **11**, 545–553.
48 S. H. Choi, J. H. Kim, J. Ahn, T. Kim, Y. Jung, D. Won, J. Bang, K. R. Pyun, S. Jeong, H. Kim, Y. G. Kim and S. H. Ko, *Nat. Mater.*, 2024, **23**, 834–843.
49 J. R. Gissinger, B. D. Jensen and K. E. Wise, *Macromolecules*, 2020, **53**, 9953–9961.
50 K.-H. Lin, L. Paterson, F. May and D. Andrienko, *Npj Comput. Mater.*, 2021, **7**, 1–7.
51 M. Klajmon, V. Aulich, J. Ludík and C. Červinka, *Ind. Eng. Chem. Res.*, 2023, **62**, 21437–21448.
52 K. S. Khare and F. R. Phelan, *Macromolecules*, 2018, **51**, 564–575.
53 M. A. Webb, Y. Jung, D. M. Pesko, B. M. Savoie, U. Yamamoto, G. W. Coates, N. P. Balsara, Z.-G. Wang and T. F. Miller, *ACS Cent. Sci.*, 2015, **1**, 198–205.
54 A. P. Thompson, H. M. Aktulga, R. Berger, D. S. Bolintineanu, W. M. Brown, P. S. Crozier, P. J. in't Veld, A. Kohlmeyer, S. G. Moore, T. D. Nguyen, R. Shan, M. J. Stevens, J. Tranchida, C. Trott and S. J. Plimpton, *Comput. Phys. Commun.*, 2022, **271**, 108171.
55 D. van der Spoel, E. Lindahl, B. Hess, G. Groenhof, A. E. Mark and H. J. C. Berendsen, *J. Comput. Chem.*, 2005, **26**, 1701–1718.
56 W. L. Jorgensen, D. S. Maxwell and J. Tirado-Rives, *J. Am. Chem. Soc.*, 1996, **118**, 11225–11236.
57 G. A. Kaminski, R. A. Friesner, J. Tirado-Rives and W. L. Jorgensen, *J. Phys. Chem. B*, 2001, **105**, 6474–6487.
58 W. Humphrey, A. Dalke and K. Schulten, *J. Mol. Graphics*, 1996, **14**(33–38), 27.
59 M. Brehm and B. Kirchner, *J. Chem. Inf. Model.*, 2011, **51**, 2007–2023.
60 O. S. Smart, J. G. Neduvelil, X. Wang, B. A. Wallace and M. S. Sansom, *J. Mol. Graphics*, 1996, **14**(354–360), 376.
61 R. A. Marcus and N. Sutin, *Biochim. Biophys. Acta, Bioenerg.*, 1985, **811**, 265–322.
62 R. A. Marcus, *Angew. Chem., Int. Ed. Engl.*, 1993, **32**, 1111–1121.
63 V. Rühle, A. Lukyanov, F. May, M. Schrader, T. Vehoff, J. Kirkpatrick, B. Baumeier and D. Andrienko, *J. Chem. Theory Comput.*, 2011, **7**, 3335–3345.
64 E. F. Valeev, V. Coropceanu, D. A. da Silva Filho, S. Salman and J.-L. Brédas, *J. Am. Chem. Soc.*, 2006, **128**, 9882–9886.
65 J. Kirkpatrick, *Int. J. Quantum Chem.*, 2008, **108**, 51–56.
66 R. Herzhoff, F. Negri, K. Meerholz and D. Fazzi, *J. Mater. Chem. C*, 2023, **11**, 11969–11979.
67 S. F. Nelsen, S. C. Blackstock and Y. Kim, *J. Am. Chem. Soc.*, 1987, **109**, 677–682.
68 J.-D. Chai and M. Head-Gordon, *Phys. Chem. Chem. Phys.*, 2008, **10**, 6615–6620.
69 T. Clark, J. Chandrasekhar, G. W. Spitznagel and P. V. R. Schleyer, *J. Comput. Chem.*, 1983, **4**, 294–301.
70 B. P. Pritchard, D. Altarawy, B. Didier, T. D. Gibson and T. L. Windus, *J. Chem. Inf. Model.*, 2019, **59**, 4814–4820.
71 R. Krishnan, J. S. Binkley, R. Seeger and J. A. Pople, *J. Chem. Phys.*, 1980, **72**, 650–654.
72 T. A. Manz and N. G. Limas, *RSC Adv.*, 2016, **6**, 47771–47801.
73 C. Bannwarth, S. Ehlert and S. Grimme, *J. Chem. Theory Comput.*, 2019, **15**, 1652–1671.
74 P. Pracht, S. Grimme, C. Bannwarth, F. Bohle, S. Ehlert, G. Feldmann, J. Gorges, M. Müller, T. Neudecker, C. Plett, S. Spicher, P. Steinbach, P. A. Wesołowski and F. Zeller, *J. Chem. Phys.*, 2024, **160**, 114110.
75 M. J. Frisch, G. W. Trucks, H. B. Schlegel, G. E. Scuseria, M. A. Robb, J. R. Cheeseman, G. Scalmani, V. Barone, G. A. Petersson, H. Nakatsuji, X. Li, M. Caricato, A. V. Marenich, J. Bloino, B. G. Janesko, R. Gomperts, B. Mennucci, H. P. Hratchian, J. V. Ortiz, A. F. Izmaylov, J. L. Sonnenberg, D. Williams-Young, F. Ding, F. Lipparini, F. Egidi, J. Goings, B. Peng, A. Petrone, T. Henderson, D. Ranasinghe, V. G. Zakrzewski, J. Gao, N. Rega, G. Zheng, W. Liang, M. Hada, M. Ehara, K. Toyota, R. Fukuda, J. Hasegawa, M. Ishida, T. Nakajima, Y. Honda, O. Kitao, H. Nakai, T. Vreven, K. Throssell, J. A. Montgomery, Jr., J. E. Peralta, F. Ogliaro, M. J. Bearpark, J. J. Heyd, E. N. Brothers, K. N. Kudin, V. N. Staroverov, T. A. Keith, R. Kobayashi, J. Normand, K. Raghavachari, A. P. Rendell, J. C. Burant, S. S. Iyengar, J. Tomasi, M. Cossi, J. M. Millam, M. Klene, C. Adamo, R. Cammi, J. W. Ochterski, R. L. Martin, K. Morokuma, O. Farkas, J. B. Foresman and D. J. Fox, *Gaussian16*, Gaussian, Inc., Wallingford CT, *2016*.
76 A. L. Rohl and D. M. P. Mingos, *J. Chem. Soc., Dalton Trans.*, 1992, 3541.
77 D. Diddens, E. Paillard and A. Heuer, *J. Electrochem. Soc.*, 2017, **164**, E3225–E3231.
78 D. Diddens and A. Heuer, *ACS Macro Lett.*, 2013, **2**, 322–326.

79 H. Bässler, *Phys. Status Solidi B*, 1993, **175**, 15–56.
80 F.-J. Kahle, A. Rudnick, S. Wedler, R. Saxena, R. Ammenhäuser, U. Scherf, S. Bagnich, H. Bässler and A. Köhler, *Adv. Energy Mater.*, 2022, **12**, 2103063.
81 T. Meier, H. Bässler and A. Köhler, *Adv. Opt. Mater.*, 2021, **9**, 2100115.
82 A. F. Voter, K. E. Sickafus, E. A. Kotomin and B. P. Uberuaga, *Radiation Effects in Solids*, 2007, pp. 1–23.
83 C. Poelking, E. Cho, A. Malafeev, V. Ivanov, K. Kremer, C. Risko, J.-L. Brédas and D. Andrienko, *J. Phys. Chem. C*, 2013, **117**, 1633–1640.
84 N. Gildemeister, S. Geller, R. Herzhoff, F. Negri, K. Meerholz and D. Fazzi, *Mater. Adv.*, 2024, **5**, 8475–8489.
85 T. Vehoff, B. Baumeier, A. Troisi and D. Andrienko, *J. Am. Chem. Soc.*, 2010, **132**, 11702–11708.
86 N. E. Jackson, L. X. Chen and M. A. Ratner, *Proc. Natl. Acad. Sci. U. S. A.*, 2016, **113**, 8595–8600.
87 B. M. Savoie, K. L. Kohlstedt, N. E. Jackson, L. X. Chen, M. La Olvera de Cruz, G. C. Schatz, T. J. Marks and M. A. Ratner, *Proc. Natl. Acad. Sci. U. S. A.*, 2014, **111**, 10055–10060.
88 N. E. Jackson, B. M. Savoie, L. X. Chen and M. A. Ratner, *J. Phys. Chem. Lett.*, 2015, **6**, 1018–1021.

